Journal of Computational Physics 229 (2010) 6915–6930

Contents lists available at ScienceDirect

Journal of Computational Physics

journal homepage: www.elsevier.com/locate/jcp

Level-set based topology optimization for electromagnetic dipole antenna design

Shiwei Zhou, Wei Li, Qing Li *

School of Aerospace, Mechanical and Mechatronic Engineering, The University of Sydney, Sydney, NSW 2006, Australia

ARTICLE INFO

Article history:
Received 29 September 2009
Received in revised form 25 May 2010
Accepted 25 May 2010
Available online 1 June 2010

Keywords:
Electric Field Integral Equation
Dipole antenna
Level-set method
Topology optimization
Shape derivative
Electromagnetic system

ABSTRACT

This paper presents a level-set framework for a typical electromagnetic design problem of dipole antenna. In this study, the geometrical configuration of an antenna is represented by the zero-level contour of a higher-dimensional level-set function. The governing equation for the induced current flow on a metal surface is the Electric Field Integral Equation (EFIE), which takes into account the electric component of the incident wave. The design objective is formulated in terms of the surface current and incident electric field. The normal velocity of the level-set model, which reflects the sensitivity of the objective function, is derived from the adjoint variable method and shape derivative. By optimizing the objective function, the area with the highest current density, to which the voltage feeding should be applied, can be reshaped. The advantages of adopting the level-set technique for electromagnetic design lie in its capacity for capturing sophisticated topological changes and facilitation in mathematical representation of the design configuration. The demonstrative examples of dipole antenna design show that the level-set method results in a fairly smooth optimization process, where the vacuum/metal interface gradually attains its optimal configuration. A series of design cases with self-adjoint and non-self-adjoint sensitivity analyses are studied and compared to the benchmarking problems in dipole antenna.

1. Introduction

The interest in designing antennae for more effectively receiving/reflecting electromagnetic signals has never ceased since the well-known Maxwell's theory was established. Particularly, over the past 30 years, it was fueled by the significant growing demands for mobile telecommunication devices and rapid development of various powerful numerical methods, such as Moment of Method (MoM) [1], Finite Element Method (FEM) [2] and Finite-Difference Time-Domain method (FDTD) [3], which allow the Maxwell's equations to be solved effectively for various frequencies. These techniques converted the antenna design from an original "cut and try" process to an elegant engineering art with substantially shorter time and lower cost [4]. One of the most popular methods in analyzing the properties of antenna with complex geometrical configuration has been the Integral Equation (IE) method, which is specifically defined as the Electric Field Integral Equation (EFIE) with the boundary condition related to the total tangential electric field [5]. Derived from the Maxwell's equation, EFIE has played a fundamental role in antenna design analysis [4,6] due to its superior capacity of obtaining the induced current density through the MoM technique [1].

Since the current density largely depends on the geometry of the antenna, its design has drawn considerable attention in topology optimization community recently. The earliest study on antenna topology optimization could be the one carried

* Corresponding author. Tel.: +61 2 9351 8607; fax: +61 2 9351 7060.
E-mail address: Qing.Li@Sydney.edu.au (Q. Li).

0021-9991/$ - see front matter © 2010 Elsevier Inc. All rights reserved.
doi:10.1016/j.jcp.2010.05.030

out by Kiziltas et al. [7] in 2003, who optimized the material configuration for antenna patch and claimed the optimized bandwidth increases 2.5 times. Lately, Nomura et al. applied this method to the design of dielectric resonator antennas in the frequency domain and successfully enhanced the bandwidths [8]. In these two studies, the antenna was modeled by the density-based Solid Isotropic Material with Penalization (SIMP) method [9], in which the presence or absence of materials was denoted by elemental relative density in either 1 (metal) or 0 (vacuum/air), respectively. To make the optimization well-posed, the discretized {0,1} density is usually relaxed to continuous [0 1] density in the optimization [9,10]. However, such a relaxation could lead to an ambiguous representation (i.e. intermediate density, neither 0 nor 1) in the optimal structures. For this reason, some special techniques like the exponential penalization on the relative density in SIMP [10] or nonlinear diffusion [11] were developed to deal with this problem. Despite some preliminary work in literature [7,8], there is a lack of continuous research. Due to a strong demand in antenna design and its potential extension to other relevant areas in electromagnetism, such as the designs of metamaterials [12] and waveguide devices, further studies are indeed needed in this highly promising area.

Being an effective method, topology optimization has been developed as a powerful tool capable of seeking the optimal configuration for a range of engineering problems in structural, fluidic, thermal and electromagnetic areas [10,13–16]. In general, there are two classes of topological models available. The first, as abovementioned, represents the geometrical configuration of the structures in terms of relative density in an explicit fashion. The SIMP [9] and Evolutionary Structural Optimization (ESO) [17] are two representative techniques in this category. The second embodies the structural layout with a zero-level contour of a higher-dimensional scalar function in an implicit fashion. The level-set technique established by Osher and Sethian [18] is one such powerful approach. Since this method can unambiguously represent the geometrical shape and is capable of effectively tracking the dynamically-moving interfaces, its breadth of applications has been extensively evidenced in the literature [19–21], including various structural optimization [22–24], metamaterial design [25] and inverse scattering problems (shape reconstruction from scattered waves) [26,27]. However, limited studies are currently available in the level-set based topology optimization for electromagnetic antenna design.

As one of the most typical examples in electromagnetism, the design of dipole antennas signifies a class of interesting problems with considerable theoretical and practical values. The conventional dipole antennas usually consist of two bilaterally symmetrical conductive arms separated by an insulator at the symmetric point. The bandwidth of such antennas is closely related to the geometrical configuration of the arms. In fact, the names of several classical dipole antennae are derived from their arm shape, such as rod, tapered and triangular dipole antennas (Fig. 1). It should be noted that the antennas in Fig. 1b and c have a much wider bandwidth than that in Fig. 1a due to their non-rectangular shapes. One effective approach to the design of the dipole antenna is to find the optimal geometrical configuration for the arms, so that the symmetric point, to which the voltage feeding is applied, has the highest current density. Other methods for dipole antenna design are also available, but beyond the scope of this paper. Interested readers can consult the literature [4] for more information in this regard.

In the level-set model, the design domains occupied by two phases, namely the vacuum space and metal, are implicitly expressed by a level-set function, which takes positive or negative value for them, respectively. The surface current is induced by the incoming incident wave and governed by EFIE [5]. In this paper, the cost function is defined as the inner product of the surface current and incident electric field to facilitate the optimization. However, to demonstrate the effectiveness of level-set framework for antenna design with different meaningful objectives, we also used the current density as a cost function in some of numerical tests. The sensitivity of the objective function with respect to the change in metal configuration is derived from the adjoint variable method and shape derivative, which defines the normal velocity to drive the level-set model toward an optimum. The EFIE and its adjoint system used for the sensitivity analysis will be solved by MoM [1], in which the solid (metal) phase is discretized into adaptive triangular mesh. Unlike traditional size and shape optimization reported in antenna design literature, the present level-set based technique optimizes the size, shape and topology of the metal structure concurrently. The illustrative examples demonstrate that such a formulation is capable of generating the part with the highest current density properly.

The organization of this paper is as follows. Following this introduction, Section 2 briefly reviews the scattering problem of EFIE and then introduces the adjoint variable method and shape derivative in electromagnetic problems. Section 3 presents the level-set model and associated numerical issues. Section 4 demonstrates two classes of examples starting from different initial designs to validate the effectiveness of this method. Finally, Section 5 draws some concluding remarks.

2. Scattering problem and sensitivity analysis

Consider an arbitrarily-shaped metal object that occupies domain Ω and is embedded in a homogeneous medium with constant permittivity ε_0 and permeability μ_0. It is assumed that this object is excited by an incoming wave (Fig. 2) and thus

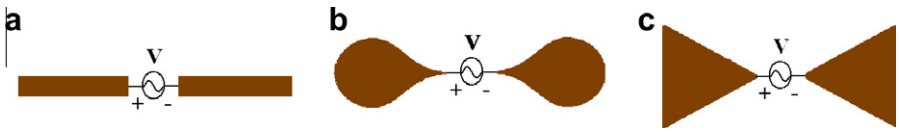

Fig. 1. The schematic configuration for (a) rod; (b) tapered; (c) triangular dipole antennas.

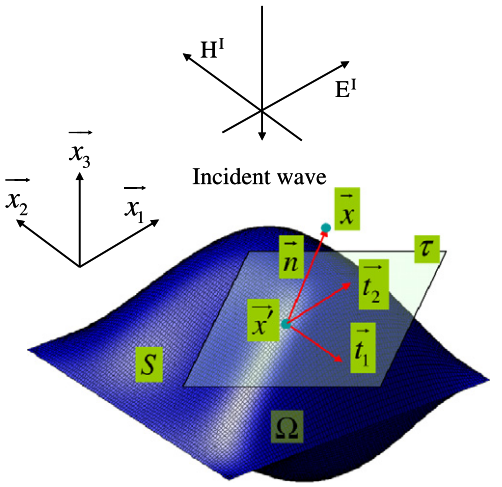

Fig. 2. The schematic of a metal object incited by a beam of wave. ($\vec{n}$ and τ denote the unit outward-pointing normal and tangent plane, respectively).

current flow $\vec{u}$ will be induced on the metal surface $\partial\Omega$. Based on the equivalent principle and the given boundary conditions, Maue established the Electric Field Integral Equation (EFIE) [5] to represent the scattered electric field E^s within the conductive object, given by

$$\vec{E}^s(\vec{x}) = -j\omega\vec{A}(\vec{x}) - \overrightarrow{\nabla V}(\vec{x}) \quad \vec{x} \in \Omega \tag{1}$$

where $j = \sqrt{-1}$, the magnetic vector potential $\vec{A}$ and scalar potential V are defined in terms of the surface integrals, respectively, as

$$\vec{A}(\vec{u},\vec{x}) = \frac{\mu_0}{4\pi}\int_{\partial\Omega}\vec{u}G(\vec{x},\vec{x}')ds \tag{2}$$

$$V(\vec{u},\vec{x}) = \frac{1}{4\pi\varepsilon_0}\int_{\partial\Omega}\sigma(\vec{u})G(\vec{x},\vec{x}')ds \tag{3}$$

The Green's function $G(\vec{x},\vec{x}') = e^{-jkR(\vec{x})}/R(\vec{x})$, which is related to the distance $R = |\vec{x} - \vec{x}'|$ between an observation point $\vec{x}$ and a source point $\vec{x}' \in \partial\Omega$, is associated with the wave number $k = \omega\sqrt{\mu_0\varepsilon_0} = 2\pi/\lambda_0$, where ω and λ_0 refer to the frequency and wavelength of the incident wave, respectively. The dependence of the surface charge density σ on the current is expressed by the surface continuity equation, given by

$$\nabla_s \cdot \vec{u} + j\omega\sigma = 0 \quad \vec{x} \in \partial\Omega \tag{4}$$

with the surface divergence operator $\nabla_s \cdot = \partial\vec{t}_1/\partial x_1 + \partial\vec{t}_2/\partial x_2$, where $\vec{t}_1$ and $\vec{t}_2$ are two orthogonal unit vectors on tangent plane τ (Fig. 2). From Eq. (4), the scalar potential in Eq. (3) becomes

$$V(\vec{u},\vec{x}) = \frac{j}{4\pi\omega\varepsilon_0}\int_{\partial\Omega}\nabla_s \cdot \vec{u}G(\vec{x},\vec{x}')ds \tag{5}$$

The projection of total electric field $\vec{E} = \vec{E^S} + \vec{E^I}$, namely the summation of the scattered and incident fields, vanishes on the tangential surface, leading to

$$\vec{n} \times \vec{E} = \vec{n} \times (\vec{E^S} + \vec{E^I}) = 0 \quad \vec{x} \in \partial\Omega \tag{6}$$

Thus the EFIE equation becomes

$$\vec{n} \times \vec{E^I} = \vec{n} \times (j\omega\vec{A}(\vec{u}) + \overrightarrow{\nabla V}(\vec{u})) \quad \vec{x} \in \partial\Omega \tag{7}$$

in which we drop the dependency on $\vec{x}$ for conciseness. In addition, the normal component of the currents vanishes on surface $\partial\Omega$, leading to $\vec{u} \cdot \vec{n} = 0$.

Multiplying a testing linear vector defined in tangential space $\{\vec{v} : \vec{v} \in W^{1,\infty}, \vec{v} \in \tau\}$ ($W^{1,\infty}$ is the first-order Sobolev space), one can obtain the weak form of EFIE given by

$$\left\langle \vec{v}, \vec{n} \times \vec{E^I} \right\rangle = j\omega\left\langle \vec{v}, \vec{n} \times \vec{A}(\vec{u}) \right\rangle + \left\langle \vec{v}, \vec{n} \times \overrightarrow{\nabla V}(\vec{u}) \right\rangle \tag{8}$$

in which the inner product $\langle \vec{a}, \vec{b} \rangle = \langle \vec{a}, \vec{b} \rangle_{\partial\Omega} = \int_{\partial\Omega} \vec{a} \cdot \vec{b} ds$ denotes an integration over the surface $\vec{x} \in \partial\Omega$ (for the conciseness of expression, the subscript $\partial\Omega$ is dropped in the formulae).

To observe the sensitivity of this weak form of EFIE with respect to the geometrical change of the solid (metal) phase, we define a potential function as

$$P(\vec{u}, \vec{v}, \partial\Omega) = -\left\langle \vec{v}, \vec{n} \times \vec{E^I} \right\rangle + j\omega \left\langle \vec{v}, \vec{n} \times \vec{A}(\vec{u}) \right\rangle + \left\langle \vec{v}, \vec{n} \times \overrightarrow{\nabla V}(\vec{u}) \right\rangle \tag{9}$$

If the domain Ω changes to $\Omega_{t_1} = \Omega + \delta\Omega = (\mathbf{I} + (t_1 - t)\vec{\theta})\Omega$ along the direction $\vec{\theta} \in W^{1,\infty}$ from time t to t_1, its surface $\partial\Omega$ changes correspondingly to $\partial\Omega_{t_1} = \partial\Omega + \delta\partial\Omega$, where symbol $\mathbf{I}$ stands for an identity. Within the time increment $\Delta t = t_1 - t$, the time limit of the difference of the first term on the right-hand side of Eq. (9) vanishes as the incident electric field E^I is invariant over the domain, given by

$$\lim_{t\to 0} -\frac{1}{t}\left(\left\langle \vec{v}, \vec{n} \times \vec{E^I} \right\rangle_{\partial\Omega_{t_1}} - \left\langle \vec{v}, \vec{n} \times \vec{E^I} \right\rangle \right) = 0 \tag{10}$$

By taking into account $\vec{a} \cdot (\vec{b} \times \vec{c}) = \vec{b} \cdot (\vec{c} \times \vec{a}) = \vec{c} \cdot (\vec{a} \times \vec{b})$, the time limit of the second term in Eq. (9) is given by

$$\begin{aligned}
&\lim_{t\to 0} \frac{j\omega}{t}\left(\left\langle \vec{v}, \vec{n} \times \vec{A}(\overrightarrow{u(t_1)}) \right\rangle_{\partial\Omega_{t_1}} - \left\langle \vec{v}, \vec{n} \times \vec{A}(\overrightarrow{u(t)}) \right\rangle \right) \\
&= \lim_{t\to 0} \frac{j\omega}{t}\left(\left\langle \vec{v}, \vec{n} \times \vec{A}(\overrightarrow{u(t_1)}) \right\rangle - \left\langle \vec{v}, \vec{n} \times \vec{A}(\overrightarrow{u(t)}) \right\rangle \right) - \lim_{t\to 0} \frac{j\omega}{t} \left\langle \vec{v}, \vec{n} \times \vec{A}(\overrightarrow{u(t_1)}) \right\rangle_{\partial(\delta\Omega)} \\
&\approx \lim_{t\to 0} \frac{j\omega\mu_0}{4\pi t}\left(\left\langle \vec{v} \times \vec{n}, \int_{\partial\Omega_1} \overrightarrow{u(t_1)} G ds \right\rangle - \left\langle \vec{v} \times \vec{n}, \int_{\partial\Omega} \overrightarrow{u(t)} G ds \right\rangle \right) \\
&\approx \frac{j\omega\mu_0}{4\pi} \left\langle \vec{v} \times \vec{n}, \int_{\partial\Omega} (\lim_{t\to 0}(\overrightarrow{u(t_1)} - \overrightarrow{u(t)})/t) G ds \right\rangle \\
&= \frac{j\omega\mu_0}{4\pi} \left\langle \vec{v} \times \vec{n}, \int_{\partial\Omega} \vec{u}_{,\partial\Omega} G ds \right\rangle
\end{aligned} \tag{11}$$

with $\overrightarrow{u}_{,\partial\Omega} = \lim_{t\to 0}(\overrightarrow{u(t_1)} - \overrightarrow{u(t)})/t$. Since $\int_{\partial\Omega} \overrightarrow{\nabla f} \cdot \vec{b} ds = -\int_{\partial\Omega} f \nabla_s \cdot \vec{b} ds + \int_{\partial\Omega} \nabla_s \cdot (f\vec{b}) ds$, we obtain

$$\begin{aligned}
\left\langle \vec{v}, \vec{n} \times \overrightarrow{\nabla V}(\vec{u}) \right\rangle &= \frac{j}{4\pi\omega\varepsilon_0} \left\langle \vec{v}, \vec{n} \times \overrightarrow{\nabla(\langle \nabla_s \cdot \vec{u}, G \rangle)} \right\rangle = \frac{j}{4\pi\omega\varepsilon_0} \left\langle \vec{v} \times \vec{n}, \overrightarrow{\nabla(\langle \nabla_s \cdot \vec{u}, G \rangle)} \right\rangle \\
&= \frac{j}{4\pi\omega\varepsilon_0} (-\langle \langle \nabla_s \cdot \vec{u}, G \rangle, \nabla_s \cdot (\vec{v} \times \vec{n}) \rangle + \langle 1, \nabla_s \cdot (\langle \nabla_s \cdot \vec{u}, G \rangle \vec{v} \times \vec{n}) \rangle)
\end{aligned} \tag{12}$$

The last term on the right-hand side of Eq. (12) vanishes as a closed boundary $\partial\Omega$ is considered in this paper.

Substituting Eq. (12) into the limit of the third term in Eq. (9) yields,

$$\lim_{t\to 0} \frac{1}{t}\left(\left\langle \vec{v}, \vec{n} \times \overrightarrow{\nabla V}(\vec{u}) \right\rangle_{\partial\Omega_{t_1}} - \left\langle \vec{v}, \vec{n} \times \overrightarrow{\nabla V}(\vec{u}) \right\rangle \right) = -\frac{j}{4\pi\omega\varepsilon_0} \langle \langle \nabla_s \cdot \vec{u}_{,\partial\Omega}, G \rangle, \nabla_s \cdot (\vec{v} \times \vec{n}) \rangle \tag{13}$$

Since the summation of Eqs. (10), (11) and (13) equals the shape derivative [28] of the potential function ($P_{,\partial\Omega}$) in direction $\vec{\theta}$, we can obtain,

$$\begin{aligned}
&\lim_{t\to 0} \frac{1}{t}(P(t_1) - P(t)) = P_{,\partial\Omega} \Rightarrow \left\langle \vec{\theta} \cdot \vec{n}, \partial(P(\vec{v}, \vec{u}))/\partial\vec{n} + \kappa P(\vec{v}, \vec{u}) \right\rangle \\
&\qquad = +\frac{j\omega\mu_0}{4\pi} \left\langle \vec{v} \times \vec{n}, \int_{\partial\Omega} \vec{u}_{,\partial\Omega} G ds \right\rangle - \frac{j}{4\pi\omega\varepsilon_0} (\langle \langle \nabla_s \cdot \vec{u}_{,\partial\Omega}, G \rangle, \nabla_s \cdot (\vec{v} \times \vec{n}) \rangle)
\end{aligned} \tag{14}$$

with the mean curvature calculated by $\kappa = \nabla \cdot \vec{n}$. Specially, when the P function is defined on the whole domain Ω, the shape derivative should be $P_{,\partial\Omega} = \left\langle \vec{\theta} \cdot \vec{n}, \partial P/\partial\vec{n} \right\rangle$ in Eq. (14).

Since the behavior of a dipole antenna depends on the surface current, an objective function is thus defined as the inner product between the surface current $\vec{u}$ and the incident electric field over the surface $\partial\Omega$, given by

$$J(\partial\Omega, \vec{u}) = \left\langle \overrightarrow{D(\vec{u})}, \vec{E^I} \right\rangle \tag{15}$$

The Eulerian derivative of the objective function with respect to time t is defined as

$$dJ/dt = \left\langle D(\vec{u})_{,\vec{u}} \vec{E^I}, \vec{u}_{,\partial\Omega} \right\rangle \tag{16}$$

where $D(\vec{u})_{,\vec{u}} = \partial D(\vec{u})/\partial\vec{u}$. Let $\vec{u}_{,\partial\Omega} = \vec{v}$ in Eq. (16) and make it equal to the right-hand side of Eq. (14), in which $\vec{u}_{,\partial\Omega}$ is substituted with the adjoint variable $\vec{w} = \vec{u}_{,\partial\Omega}$, thus, the adjoint problem of EFIE weak form is obtained as:

$$\frac{j\omega\mu_0}{4\pi}\left\langle \vec{v}\times\vec{n}, \int_{\partial\Omega}\vec{w}Gds\right\rangle - \frac{j}{4\pi\omega\varepsilon_0}(\langle\langle\nabla_s\cdot\vec{w}, G\rangle, \nabla_s\cdot(\vec{v}\times\vec{n})\rangle) = \left\langle D(\vec{u})_{,\vec{u}}\vec{E^I}, \vec{v}\right\rangle \tag{17}$$

The solution to the above adjoint equation, $\vec{w}$, can be used as the testing function $\vec{v}$ in $P(\vec{v},\vec{u})$ because they are in the same functional space. From Eqs. (14), (16) and (17), the variation of the objective function with respect to the boundary $\partial\Omega$ is given by

$$dJ/dt = \left\langle D(\vec{u})_{,\vec{u}}\vec{E^I}, \vec{w}\right\rangle = \left\langle \vec{\theta}\cdot\vec{n}, R(\vec{w},\vec{u})\right\rangle \tag{18}$$

with $R(\vec{w},\vec{u}) = \partial P(\vec{w},\vec{u})/\partial\vec{n} + \kappa P(\vec{w},\vec{u})$ or $R(\vec{w},\vec{u}) = \partial P(\vec{w},\vec{u})/\partial\vec{n}$. If the normal component of $\vec{\theta}$ is set as $\vec{\theta}\cdot\vec{n} = R(\vec{w},\vec{u})$, the objective function increases progressively with respect to time, as

$$J(\partial\Omega^{t+\Delta t},\vec{u}) - J(\partial\Omega^{t},\vec{u}) = \Delta t\langle R(\vec{w},\vec{u}), R(\vec{w},\vec{u})\rangle = \Delta t R^2 \geqslant 0 \tag{19}$$

3. Level-set model and numerical implementation

The level-set model and some associative numerical issues on the implementation of the aforementioned topological sensitivity analysis for dipole antenna design are discussed in this section.

3.1. Level-set model and relevant numerical issues

In the level-set technique proposed by Osher and Sethian [29], the profile of a structure is implicitly expressed by the zero-level contour of a higher-dimensional Lipschitz-continuous function $\varphi(\vec{x})$. Mathematically, the negative, zero and positive values of the level-set function divide the design domain into three territories as:

$$\varphi(\vec{x}) < 0 \quad \forall\vec{x}\in\Omega \tag{20a}$$
$$\varphi(\vec{x}) = 0 \quad \forall\vec{x}\in\partial\Omega \tag{20b}$$
$$\varphi(\vec{x}) > 0 \quad \text{otherwise} \tag{20c}$$

One of the main advantages of the level-set model is that a sophisticated shape (e.g. the head profile in Fig. 3) can be embedded in a moving surface governed by the well-know Hamilton–Jacobi (HJ) equation, as

$$\frac{\nabla\varphi}{\nabla t} + \vec{V}_n\|\nabla\varphi\| = 0 \tag{21}$$

where $\|\nabla\varphi\|$ is the norm of the level-set function. When the normal velocity $\vec{V}_n$ is coincident with the gradient direction $\vec{\theta}$ that was derived as the sensitivity in the previous section, the objective function can evolve towards an optimum.

In actual numerical implementation of the level-set algorithm, the normal velocity defined on the boundaries should be extended to

$$\vec{V}_n = \int_{\partial\Omega} R(\vec{w},\vec{u})ds = \int_{\Omega}\gamma(\varphi)\|\nabla\varphi\|R(\vec{w},\vec{u})d\Omega \tag{22}$$

where the delta function $\gamma(\varphi)$ is the derivative of the Heaviside function which takes 0 or 1 in case $\varphi < 0$ or $\varphi > 0$, respectively.

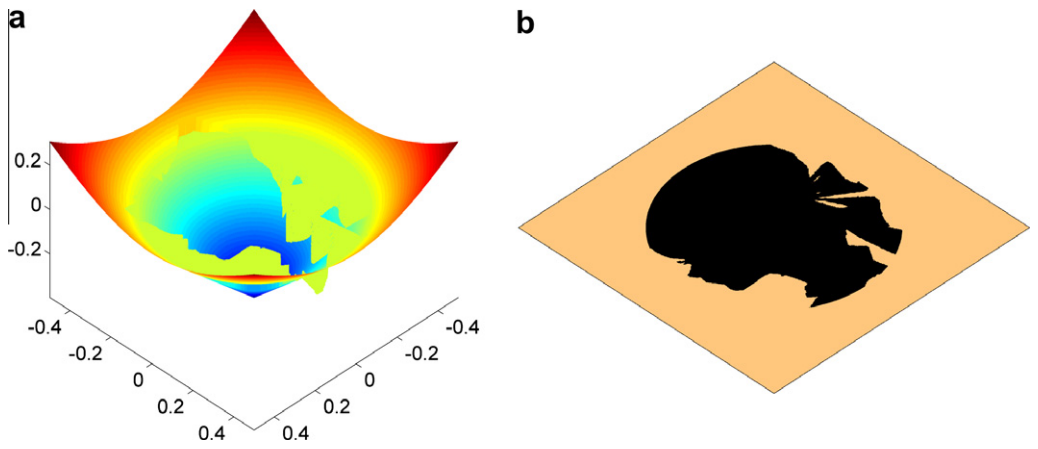

Fig. 3. The level-set function (a) and its zero-level contour (b).

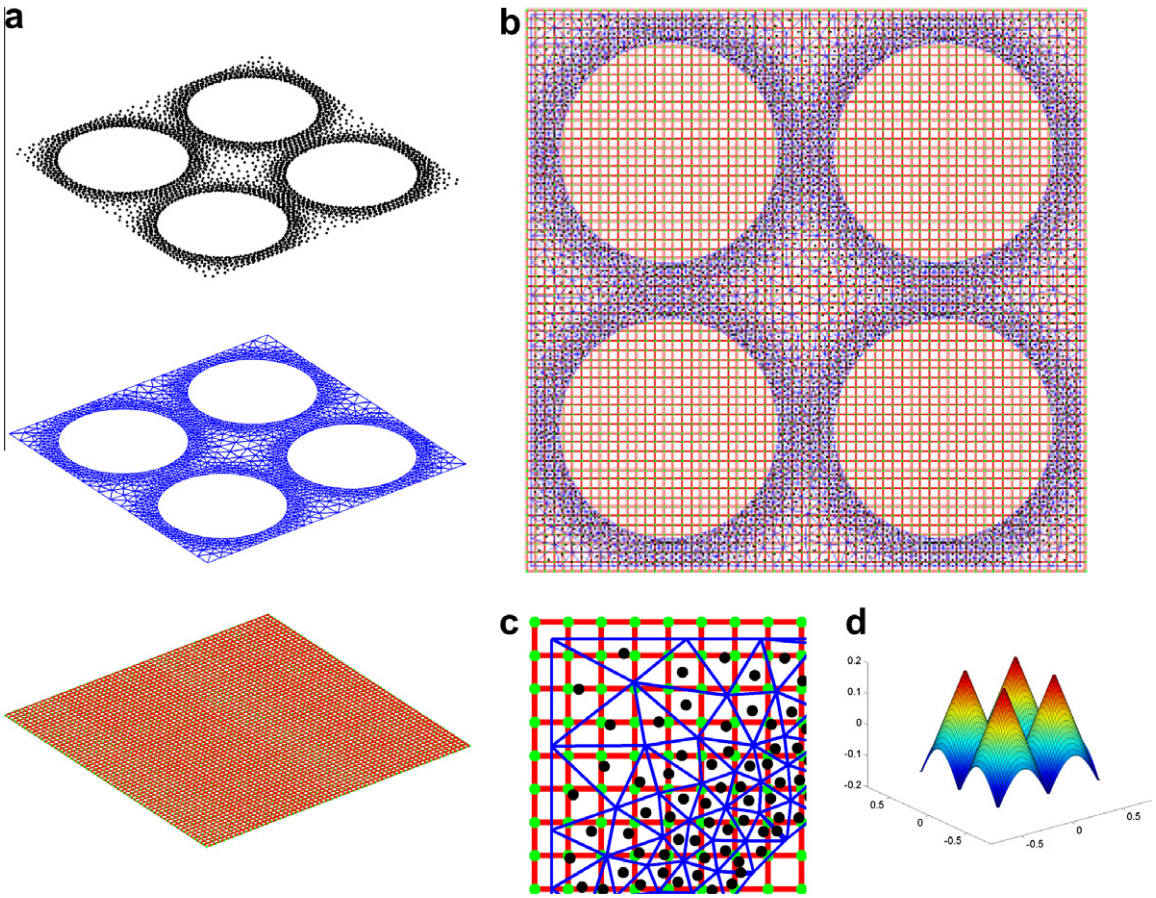

Fig. 4. The square and triangular meshes for the level-set model and EFIE-related problems: (a,b) 3D and 2D views of the two-layer mesh and the center points of the triangular mesh, (c) the zoomed-in part of subfigure b at its left-top corner and (d) the level-set function defining the design domain with four circular-shaped holes.

The numerical approaches for solving the HJ equation are widely available and we herein adopted the commonly-used upwind algorithm [29]. The design domain for the level-set model ($\{\vec{x}| - 0.5(1+h) < x_1, x_2 < 0.5(1+h)\}$) is discretized with a uniform square mesh (the red grid in Fig. 4b and c).[1] In this formulation, the two 2D coordinate components of $\vec{x}$ are denoted as x_1 and x_2, respectively. The mesh size is $h = 1/nx$ when the design domain is divided evenly into $nx = ny$ elements in the horizontal and vertical directions. The reason why the domain used for level-set model is slightly larger than the one for the antenna design ($\{\vec{x}| - 0.5 < x_1, x_2 < 0.5\}$) is that a circle of nodes (Fig. 4b and c) should be embroidered at the outmost edges of this mesh to reflect the Neumann's boundary condition properly in the level-set model. Since EFIE and its adjoint problems are solved in the triangular mesh (blue mesh in Fig. 4) according to MoM [1], the current vector and the adjoint variable at the center of the triangle elements (black dots as in Fig. 4) should be mapped back to the level-set nodes (green dots in Fig. 4) correspondingly.

Our tests revealed that the mesh quality could play a significant role in the optimization because poor meshes usually result in considerably distorted results or even singularity when solving EFIE and its adjoint systems. For instance, if the solid (metal) region (area with negative value in the level-set function) is homogeneously discretized as in Fig. 5a, the extremely high and incorrectly-pointed current flows appear (Fig. 5b) due to an obvious difficulty in capturing curved boundaries smoothly. A zoomed-in snapshot of Fig. 5b (Fig. 5c) clearly exhibits this numerical singularity. Note that in these subfigures, the magnitude of the current is proportional to the length and thickness of the arrows. Numerical examples demonstrate that such mesh quality also results in slow convergence or even divergence of the objective value. However, if the same region is discretized with an adaptive mesh (Fig. 5d), the current flows would become much more logical (Fig. 5e and f). Since there are more elements around the inner boundaries where their sizes are two or three times smaller than the rest of the parts of the metal object, the adaptive mesh represents the circular geometry in a much more precise fashion even with fewer elements in total. Fig. 5a shows that an evenly-distributed mesh with 4100 elements failed to capture the circular boundaries, while an adaptive mesh with 2987 elements in Fig. 5d can represent the curved boundaries more adequately.

[1] For interpretation of color in Figs. 4 and 7, the reader is referred to the web version of this article.

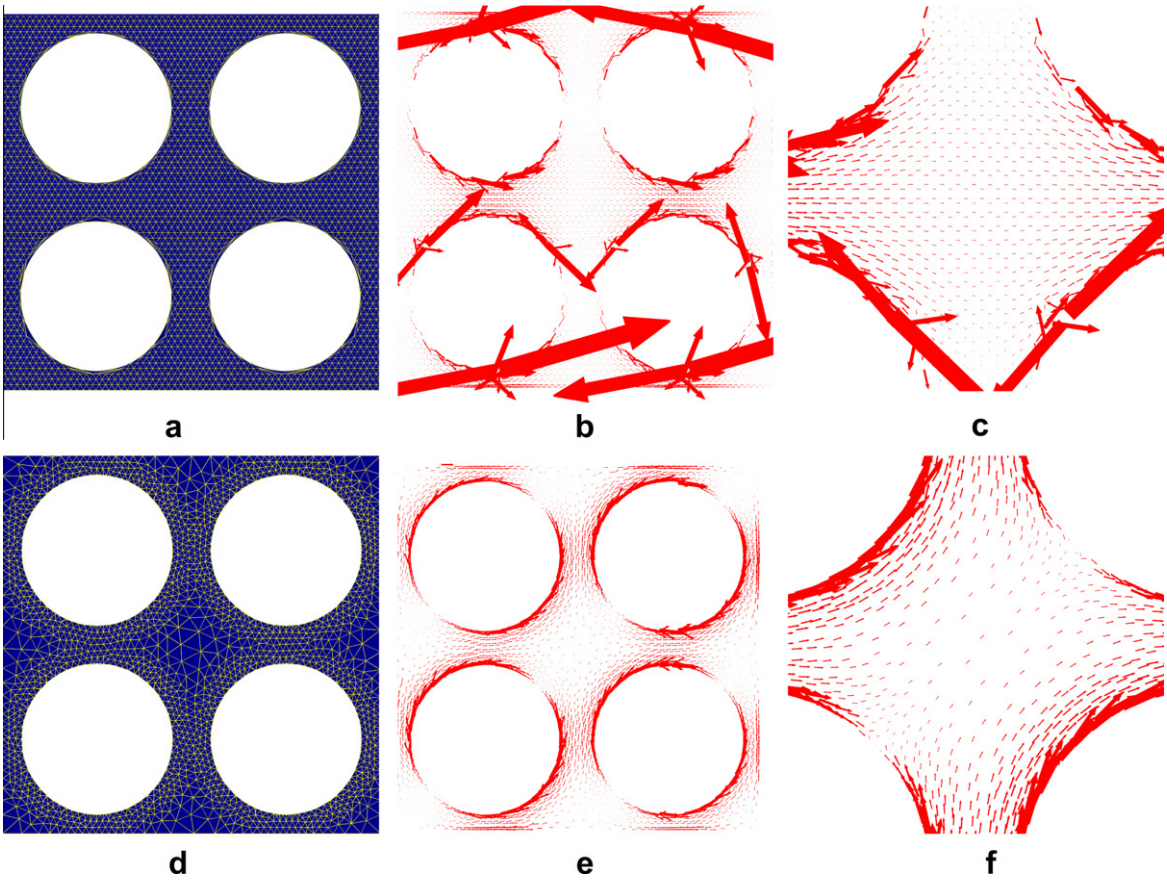

Fig. 5. The effect of mesh quality on the solutions to EFIE: (a) homogeneous mesh; (b) the singular surface current; (c) the zoomed-in image of subfigure (b) in its central part; (d) adaptive mesh; (e) the well-arranged surface current and (f) the zoomed-in image of subfigure (e) in its central part.

The adaptive mesh can be obtained by three steps: (1) obtain randomly-distributed nodes within the area occupied by metal material; (2) triangularized these nodes by Delaunay algorithm [30]; (3) update the position of nodes by forcing a truss structure to its static equilibrium at which the lengths of all bars would be nearly equal [31]. Steps 2 and 3 usually need to repeat for dozens of times before the mesh reaches a well-balanced state. In this algorithm, we relate the element size to the value of level-set function as follows:

$$h^e = h\max(0.6, \min(3, -2\varphi^e/\varphi_{\max})) \tag{23}$$

where φ^e is the value of local level-set function, h the space step of the square mesh ($h = \max(1/nx, 1/ny)$) and $\varphi_{\max}$ the maximal absolute value of the level-set function. It must be emphasized that the triangular mesh should be regenerated in each step as its hosting metal region is dynamically changing. In accordance with the upwind algorithm, the level-set function with a signed distance benefits the stability and accuracy of this movement considerably [20]. But such a desirable property could be destroyed after several evolution steps. Thus, a reinitialization process, aiming to regain the signed distance as well as maintaining the zero-level contour of the level-set function, is necessary. We herein use the reinitialization method proposed by Sussman et al. by solving another HJ equation. Interested readers are directed to the literature [32] for more detail.

3.2. Method of moment for adjoint system

Since $\vec{v} \times \vec{n}$ is located on the tangential surface, it still belongs to the testing linear vector space. Therefore, we can substitute it with $\vec{v}_m = \vec{v} \times \vec{n}$ in the adjoint equation and obtain the weak form as

$$\frac{j\omega\mu_0}{4\pi}\left\langle \vec{v}_m, \int_{\partial\Omega} \vec{w} G ds \right\rangle - \frac{j}{4\pi\omega\varepsilon_0}\left(\left\langle \langle \nabla_s \cdot \vec{w}, G\rangle, \nabla_s \cdot \vec{v}_m \right\rangle\right) = \left\langle D(\vec{u})_{,\vec{u}} \vec{E}^I, \vec{v}_m \right\rangle \tag{24}$$

The testing function can be approximated by its subspace, a piecewise continuous functional space spanned by N_e linear independent basis functions $\{\vec{b}_n(\vec{x}),\ n = 1, \ldots, N_e\}$, leading to

$$\vec{v}_m \approx \sum_{n=1}^{N_e} I_n \vec{b}_n(\vec{x}) \tag{25}$$

where unknown coefficients I_n are defined on these N_e non-boundary edges. However, it must be noted that the boundary edges are not included in Eq. (25) because the adjoint variable does not have normal components on these edges either.

In MoM, each basis function corresponds to one non-boundary edge shared by two adjacent triangles, only on which this basis function has a non-zero value. This class of basis functions was firstly proposed by Glisson [33] and has been successfully used in the solutions to the scattered problems governed by EFIE [34]. Mathematically, it is given by

$$\vec{b}_n(\vec{x}) = \begin{cases} \frac{l_n}{2A_n^{\pm}} \vec{\rho}_n^{\pm} & \vec{x} \in T_n^{\pm} \\ 0 & \vec{x} \in \partial\Omega \setminus (T_n^+ \cup T_n^-) \end{cases} \tag{26}$$

where l_n denotes the length of the common edge shared by two triangles $T_n^{\pm}$ with the area of $A_n^{\pm}$, $\vec{\rho}_n^+$ is a vector pointing from the free vertex of T_n^+ to its inner point $\vec{x} \in T_n^+$ while $\vec{\rho}_n^-$ points from the free vertex of the triangle T_n^- to point $\vec{x} \in T_n^-$.

From the definition of basis functions in Eq. (26), we obtain

$$\left\langle \vec{v}_m, \int_{\partial\Omega} \vec{w} G ds \right\rangle = \frac{1}{2} I_m l_m \left(\left\langle \int_{\partial\Omega} \vec{w} G ds, \vec{\rho}_m^+ \right\rangle_{T^+} \Big/ A_m^+ + \left\langle \int_{\partial\Omega} \vec{w} G ds, \vec{\rho}_m^- \right\rangle_{T^-} \Big/ A_m^- \right) \tag{27}$$

$$\left\langle \langle \nabla_s \cdot \vec{w}, G \rangle, \nabla_s \cdot \vec{v}_m \right\rangle = l_m I_m \left(\langle \langle \nabla_s \cdot \vec{w}, G \rangle, 1 \rangle_{T^+} / A_m^+ - \langle \langle \nabla_s \cdot \vec{w}, G \rangle, 1 \rangle_{T^-} / A_m^- \right) \tag{28}$$

$$\left\langle D'(\vec{u}) \vec{E}^I, \vec{v}_m \right\rangle = \frac{1}{2} l_m I_m \left(\left\langle D'(\vec{u}) \vec{E}^I, \vec{\rho}_m^+ \right\rangle_{T^+} \Big/ A_m^+ + \left\langle D'(\vec{u}) \vec{E}^I, \vec{\rho}_m^- \right\rangle_{T^-} \Big/ A_m^- \right) \tag{29}$$

where $\langle \vec{v}_m, \vec{a} \rangle = \frac{1}{2} l_m (\langle \vec{a}, \vec{\rho}_m^+ \rangle_{T^+} / A_m^+ + \langle \vec{a}, \vec{\rho}_m^- \rangle_{T^-} / A_m^-)$, $\langle c, \nabla_s \cdot \vec{v}_m \rangle = l_m (\langle c, 1 \rangle_{T^+} / A_m^+ - \langle c, 1 \rangle_{T^-} / A_m^-)$ [33,34]. The right-hand sides having the form $\langle \vec{a}, \vec{b} \rangle_{T^{\pm}} / A_m^{\pm}$ in Eqs. (27)–(29) are the average values within these two triangles, which can be approximated by $\langle \vec{a}, \vec{b} \rangle_{T^{\pm}} / A_m^{\pm} \approx \vec{a}(\vec{x}) \cdot \vec{b}(\vec{x})$ for $\vec{x} \in T^{\pm}$. Bringing Eqs. (27)–(29) back to Eq. (24) with $c_m^{\pm}$ standing for the center points of the mth triangle $T_m^{\pm}$, we can obtain,

$$\begin{aligned} &\frac{j\omega\mu_0}{8\pi} \left(\int_{\partial\Omega} \vec{w} G\left(\vec{x}, \vec{c}_m^+\right) ds \cdot \overrightarrow{\rho_m^+\left(\vec{c}_m^+\right)} + \int_{\partial\Omega} \vec{w} G\left(\vec{x}, \vec{c}_m^-\right) ds \cdot \overrightarrow{\rho_m^-\left(\vec{c}_m^-\right)} \right) - \frac{j}{4\pi\omega\varepsilon_0} \left(\left\langle \nabla_s \cdot \vec{w}, G\left(\vec{x}, \vec{c}_m^+\right) \right\rangle - \left\langle \nabla_s \cdot \vec{w}, G\left(\vec{x}, \vec{c}_m^-\right) \right\rangle \right) \\ &= \frac{1}{2} \left(D\left(\overrightarrow{u(\vec{c}_m^+)}\right)_{,\vec{u}} \vec{E}^I \cdot \overrightarrow{\rho_m^+\left(\vec{c}_m^+\right)} + D\left(\overrightarrow{u(\vec{c}_m^-)}\right)_{,\vec{u}} \vec{E}^I \cdot \overrightarrow{\rho_m^-\left(\vec{c}_m^-\right)} \right) \end{aligned} \tag{30}$$

By approximating $\vec{w} \approx \sum_{n=1}^{N_e} I_n \vec{b}_n(\vec{x})$, Eq. (30) is expressed as a system of linear equations given in a matrix form as

$$KI = f \tag{31}$$

where

$$f_m = \frac{1}{2} \left(D\left(\overrightarrow{u(\vec{c}_m^+)}\right)_{,\vec{u}} \vec{E}^I \cdot \overrightarrow{\rho_m^+\left(\vec{c}_m^+\right)} + D\left(\overrightarrow{u\left(\vec{c}_m^-\right)}\right)_{,\vec{u}} \vec{E}^I \cdot \overrightarrow{\rho_m^-\left(\vec{c}_m^-\right)} \right) \tag{32}$$

$$K_{mn} = \frac{j\omega\mu_0 l_n}{16\pi} \left(G(\vec{x}, \vec{c}_m^+) \overrightarrow{\rho_n^+\left(\vec{c}_n^+\right)} \cdot \overrightarrow{\rho_m^+\left(\vec{c}_m^+\right)} + G(\vec{x}, \vec{c}_m^-) \rho_n^-(\vec{c}_n^-) \cdot \overrightarrow{\rho_m^-\left(\vec{c}_m^-\right)} \right) - \frac{j l_n}{4\pi\omega\varepsilon_0} \left(G(\vec{x}, \vec{c}_m^+) - G(\vec{x}, \vec{c}_m^-) \right) \tag{33}$$

with $G(\vec{x}, \vec{c}_m^{\pm}) = \sum_{n=1}^{NE} G(\vec{c}_n^{\pm}, \vec{c}_m^{\pm})$.

Finally, it should be mentioned that the discretized value of $P_t(\vec{w}, \vec{u})$ in a triangle is defined by its three edges E_t^i, $i = 1, 2, 3$, each corresponding to two triangles ($T_t^{i\pm}$, $i = 1, 2, 3$). Mathematically, it is approximated as

$$\begin{aligned} P_t(\vec{w}, \vec{u}) &= -\vec{w}_t \cdot \vec{E}^I + j\omega \vec{w}_t \cdot \vec{A}(\vec{u}_t) + \vec{w}_t \cdot \overrightarrow{\nabla V(\vec{u}_t)} = \vec{w}_t \cdot \left(-\vec{E}^I + C_1 \int_t \vec{u}_t G ds + C_2 \overrightarrow{\nabla \int_{\partial\Omega} \nabla_s \cdot \vec{u}_t G ds} \right) \\ &= \overrightarrow{W}_t \cdot \left(-\vec{E}^I + C_1 \sum_{e=E_t^1}^{E_t^3} \frac{l^e I^e}{2} \left(\vec{\rho}_t^{i+} G\left(\vec{x}, \vec{c}_t^{i+}\right) + \vec{\rho}_t^{i-} G\left(\vec{x}, \vec{c}_t^{i-}\right) \right) + C_2 \overrightarrow{\nabla \left(\sum_{e=E_t^1}^{E_t^3} l^e I^e \left(G(\vec{x}, \vec{c}_t^{i+}) - G(\vec{x}, \vec{c}_t^{i-}) \right) \right)} \right) \end{aligned} \tag{34}$$

with $C_1 = \mu_0 j\omega/(4\pi)$, $C_2 = j/(4\pi\omega\varepsilon_0)$ and $\vec{W}_t = \sum_{e=E_t^1}^{E_t^3} l^e W^e / 2 (\overrightarrow{\rho_t^{i+}} / A_t^{i+} + \overrightarrow{\rho_t^{i-}} / A_t^{i-})$.

3.3. Volume constraint

Although a constraint of volume fraction V_0, namely the ratio of the area occupied by solid (metal) phase to the design domain, is not always necessary in antenna design, we still consider it in the optimization to make the design results more comparable. This is especially critical for the antennas with small volume fraction; otherwise, the optimization can be stuck

as the volume tends to zero. However, the prescription of a volume constraint often makes the optimization more sophisticated.

The Lagrangian method is one of the effective approaches to satisfy a prescribed volume constraint, by introducing a sufficiently large multiplier to the constraint function. Besides a trial of multiplier in optimization process as suggested in [22], the multiplier can be derived mathematically from the variational method [24,35,36]. Due to the first-order approximation in the derivation, the multiplier needs to be rectified with some proper algorithms (e.g. Newtown method), otherwise the volume constraint will be ruined eventually [35,36].

In this paper, we would like to adopt the bisection algorithm from the literature [35,37], which is heuristic in nature but relatively simple, stable and efficient. This algorithm was originally used in density-based topology optimization [38] and extended to the level-set models recently [35,37]. The key idea of this algorithm is to reduce the multiplier bisectionally. For example, the original value is bounded by $-\infty < l_1^0 \ll l_2^0 < \infty$. Then a testing Lagrange multiplier $\lambda^0 = 0.5(l_1^0 + l_2^0)$ is used to evaluate the variation of the level-set function $\delta\varphi = (\lambda + \vec{V}_n)\|\nabla\varphi\|$, with which the new metal volume V_0^1 is calculated in terms of the increment $\varphi^{m+1} = \varphi^m + \delta\varphi^m$ (m denotes the iteration step). If the new volume is larger than V_0, then λ^0 is set as the lower bound l_1^1, otherwise set as the upper bound l_2^1. In this process, the bound becomes one-half of the original one in each iteration so that it can converge fairly quickly.

3.4. Dynamic approximation of the Heaviside function

The theoretically discontinuous Heaviside function (jump from 0 to 1 suddenly at $\varphi = 0$) can be approximated by a continuous function to avoid singularity in numerical implementation [29]. In this paper, the following first-order approximation is used as

$$H(\varphi) = \begin{cases} 0 & \varphi < -\eta \\ (1 + \varphi/\eta + \sin(\pi\varphi/\eta)/\pi)/2 & \text{otherwise} \\ 1 & \varphi > \eta \end{cases} \tag{35}$$

where η depends on the space step h of the level-set upwind algorithm [29] and denotes the half width of a transition band, in which $H(\varphi)$ changes from 0 to 1 gradually. It can be difficult to define a proper band width because a wide band could generate an inaccurate normal velocity, leading to unexpected rupture of the structure at sensible location and causing a sudden drop of the objective function, while a narrow band can slow down the convergence. To avoid such drawbacks, the band width is dynamically changed in the optimization as follows: (1) a large-enough band width is defined initially to enable the algorithm to converge quickly; (2) when the objective is substantially smaller than the former one in iteration m, which likely indicates that a rupture could be occurring, the level-set function φ is rolled back to its previous value in step m-2. At the same time, the band width is decreased slightly. With this improvement, the fluctuation of the objective function can be avoided while keeping a proper convergent speed.

4. Demonstrative examples

The solution to the adjoint sensitivity problem makes the optimization fairly challenging. But it is possible to make it self-adjoint (i.e. the adjoint variable equals the solution to EFIE) by defining a special objective function similar to the mean compliance in structural topology optimization problems [22] and the dissipation energy in fluid problems [35]. To obtain a self-adjoint optimization problem, simply setting $D(\vec{u}) = \vec{u}$ in the objective function can make the right-hand side of the weak form of the adjoint system (Eq. (17)) have the same form as that of the EFIE equation, namely $\langle D(\vec{u})_{,\vec{u}} E^I, \vec{v}\rangle = \langle E^I, \vec{v}\rangle$. Mathematically, this objective function is given as

$$J(\partial\Omega, \vec{u}) = \left\langle \vec{u}, \vec{E^I} \right\rangle \tag{36}$$

It must be pointed out that this objective function bears a considerable equivalence to the current density because the current flow is parallel to the incident electrical field at the metal surface except on some boundaries. Unlike other physical properties such as the radiation pattern, gain and bandwidth that are often used to evaluate the performance in various antennas, the properly-distributed current density on the metal surface does not seem to be a direct goal in antenna design. It is however a basis for all those properties as it is directly induced by the incident wave and consequently determines the electromagnetic fields. Particularly for dipole antennas, the current density is rather critical as the point with the maximal current density is often the location to form a gap, across which the voltage difference reflecting the signal reception is maximized [39].

In all the following examples, the incident wave propagates along $-x_3$ direction and the electric component along x_1 axis (Fig. 6), namely $E^{inc} = e^{-jkz}[1 \quad 0 \quad 0]^T$. It is assumed that the wavelength is 10, much larger than the unit squared design domain ranging from −0.5 to 0.5. Since we only consider the 2D examples in this paper, the objective function is defined as an integral over Ω, resulting in $R(\vec{w}, \vec{u}) = \partial P(\vec{w}, \vec{u})/\partial\vec{n}$.

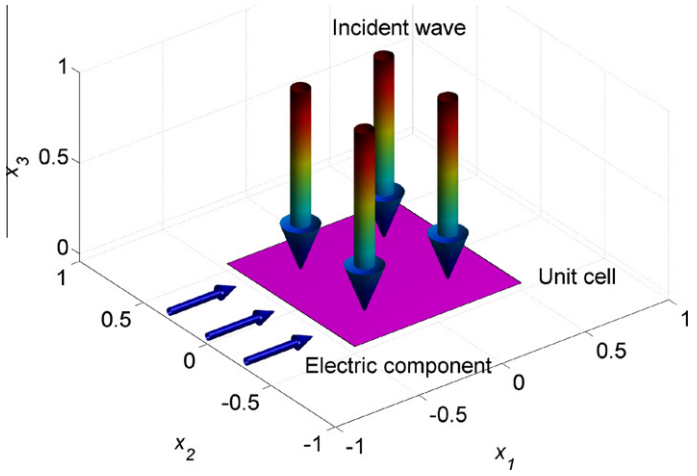

Fig. 6. The antenna incited by the horizontal (x_1) incident waves with only electric component.

4.1. Self-adjoint example

The first example (Case 1) considers a design process starting from a circular metal object (Fig. 7a). Fig. 7 displays the progression of the objective function together with some intermediate designs that are arranged in clockwise direction corresponding to the red dots in the objective curve. The snapshots in Fig. 7 exhibit the evolution process for the solid phase (metal) with the colors indicating the normalized magnitude of the real part of current flow (red/blue represents large/small magnitude, respectively). It is observed that in this case, the circle is gradually stretched in the horizontal direction with the top and bottom parts becoming flattened in the first 10 iterations ($m = 10$, Fig. 7b). Then two small notches start emerging in the top and bottom edges ($m = 20$, Fig. 7c), where they have a higher current density (red in color or black in grey print). The notches become wider and deeper in the following iterations (i.e. $m = 30$–70, Fig. 7d–h), stretching the metal region continuously. The objective curve (Fig. 7) indicates that it rises slowly in the beginning, when there is no shallow notch. But it increases sharply when the notches become deeper, and the connector becomes thinner in the later stages (e.g. Fig. 7d–f). Quantitatively, the curve shows that the final objective is hundreds of times larger than the initial one.

The normalized mean current density distribution with respect to its depth in vertical direction (x_2) along horizontal (x_1) axis for the final result is plotted in Fig. 8a, which clearly shows that the middle part has a strong current density concentration. According to the role of dipole antenna design, the part with the highest current density should be the place where the metal object is separated to generate a gap for the input of voltage feeding (Fig. 8b) [39].

From the evolution process showed in Fig. 7, the design is purely a shape optimization as no topological change takes place throughout the process. It is the fact that this level-set method is unable to create holes in the optimization because

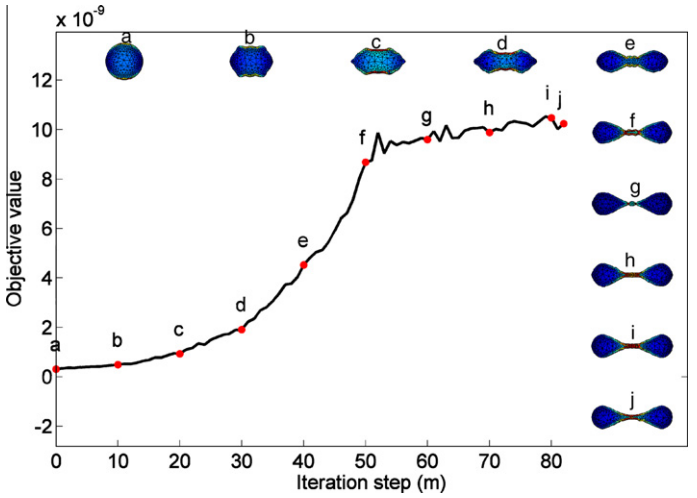

Fig. 7. The design history for the example under horizontal wave (Case 1 from the initial design with single circle).

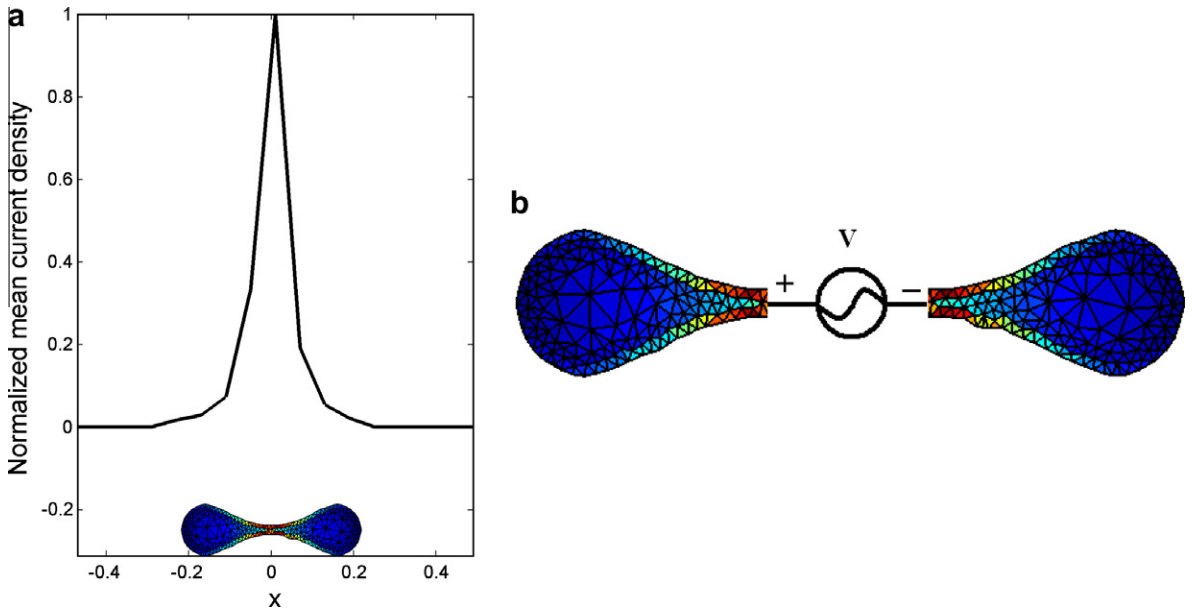

Fig. 8. (a) The current density distribution in horizontal direction and (b) the dipole antenna obtained by separating the part with maximal current density.

its normal velocity is derived in terms of the shape derivative. But when the initial structures have multiple holes or separated parts (Cases 2–6 below), the topologies can vary during the optimization with the mergence of the holes and parts. Similar initial designs have been widely used for the level-set method in structural topology optimization [24]. For this reason, we prefer using the term of "topology optimization" rather than "shape optimization with the possibility of merging holes" in the paper.

The second case (Case 2) starts from two separate identical circles with their central points located at the same height (i.e. $x_2 = 0$) (Fig. 9a). Again, the objective value rises slowly in the beginning while the two circles are stretched horizontally ($m = 0$–60 in Fig. 9a–f). As these two solids merge from Fig. 9f and g, there is a swift jump in the objective function due to such a significant topological change. Then the design optimization goes on with a further increase in the objective function, finally shaping the antenna into a long dumb-like structure (Fig. 9i). After this stage, the shape of the structure con-

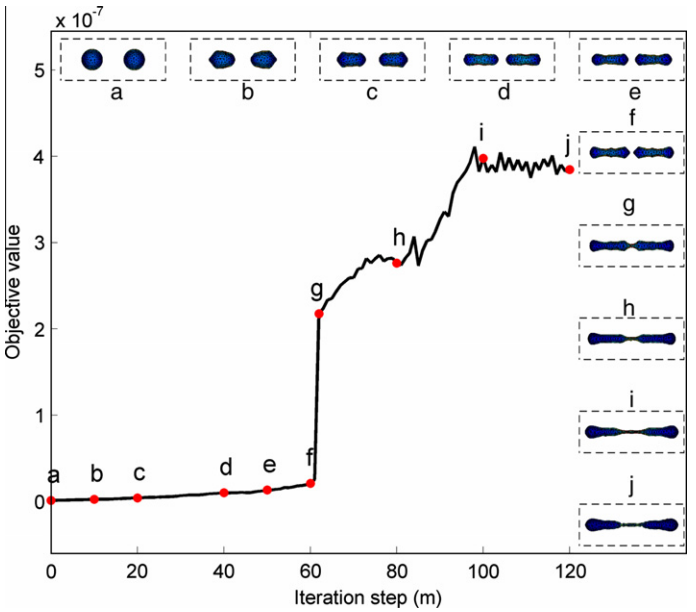

Fig. 9. The optimization history of the objective function and topological design (Case 2 from the initial design with the dual circles).

verges with a slight fluctuation of the objective from Fig. 9i and j. Similarly to the previous case, the middle part of this structure should be sectioned for voltage feeding.

To further illustrate the capability of topology optimization in this problem, the structures with multiple holes are also used as the initial designs in the following two cases (Cases 3 and 4) for the self-adjoint example. In Case 3, three initial circular holes gradually diminish and the structure takes a bar-like shape with non-uniform height in the first 80 iterations (Fig. 10a–h). Finally, the bar takes an elegant dumb-like shape with an extremely thin connector in its middle point (Fig. 10i and j). Since the side edges of the initial structure are close to the design boundaries, such solid edges reach the side boundaries quickly and stay there permanently, leaving the final structure with flat side edges. The contours in Fig. 10j indicate that the current density attains its highest value at the middle of the thin connector, which can be the voltage feeding location for the dipole antenna.

Unlike Case 3, the four initial holes (Fig. 11a) in Case 4 break from the bottom and top edges in the beginning of optimization (Fig. 11b), shaping the metal region into a fence-like structure with three bumps, respectively, at its center and two ends (Fig. 11b–f). Then the central bump diminishes gradually (Fig. 11g–i), finally becoming a flat bar connecting two elegant drop-like ends (Fig. 11j). The objective increases gradually during the optimization and converges in the final stage from Fig. 11h–j. The current density again attains its highest value in the middle of the structure, thus locating the voltage feeding here.

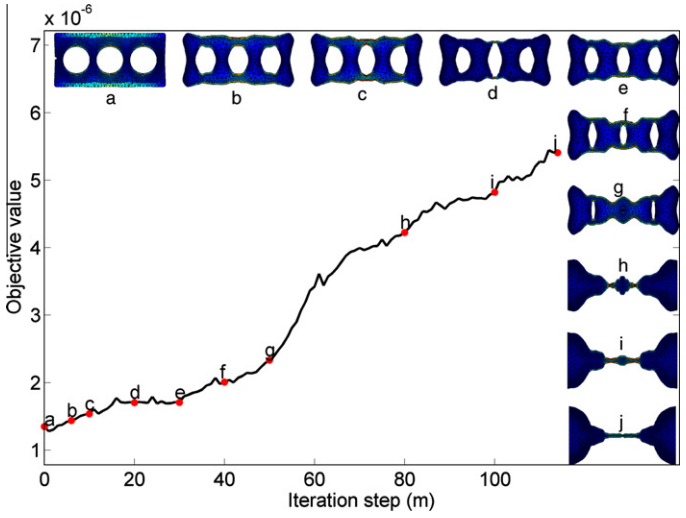

Fig. 10. The convergence of the objective function and evolution process for the example under horizontal wave (Case 3 from the initial design with three circular holes).

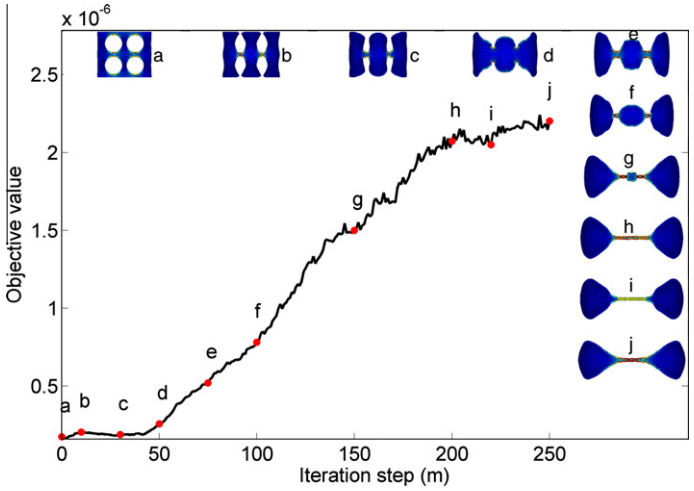

Fig. 11. Optimization history (for Case 4 induced in the horizontal wave, self-adjoint, from the initial design with four circular holes).

4.2. Non-self-adjoint example

Although some optimization problems happen to be self-adjoint, it may not always be the case. For this reason, we will demonstrate how the presented level-set framework handles the non-self-adjoint problems.

By setting the following objective function as half of the inner product of the current flow itself, namely the norm of the current density:

$$J(\partial\Omega, \vec{u}) = \frac{1}{2}\langle \vec{u}, \vec{u} \rangle \tag{37}$$

we obtain an adjoint problem according to Eq. (17)

$$\frac{j\omega\mu_0}{4\pi}\left\langle \vec{v}\times\vec{n}, \int_{\partial\Omega}\vec{w}G ds \right\rangle - \frac{j}{4\pi\omega\varepsilon_0}(\langle\langle \nabla_s\cdot\vec{w}, G\rangle, \nabla_s\cdot(\vec{v}\times\vec{n})\rangle) = \vec{u} \tag{38}$$

The weak form is presented as

$$\vec{n}\times\left(j\omega\vec{A}(\vec{w}) + \overrightarrow{\nabla V}(\vec{w})\right) = \vec{n}\times\vec{u} \quad \vec{x}\in\partial\Omega \tag{39}$$

which shows that the incident electric field on the right-hand side of EFIE will be replaced by the solution to EFIE in the adjoint system.

The first case (Case 5) of non-self-adjoint example starts from a circular object as shown in Fig. 12. Unlike what happened in Case 1 of the self-adjoint problem, the structure changes from a circle to a diamond-like shape in the initial iterations ($m = 20$). Then, the structure extends itself continuously along horizontal direction. After it reaches the side boundaries, the metal material accumulates on the boundaries, making the middle part thinner and thinner. Finally the optimization converges after 150 iterations and a dumb-like structure with two head-to-head triangular structure is generated ($m = 188$). Note that since the objective function increases thousands of times during the optimization, the convergence

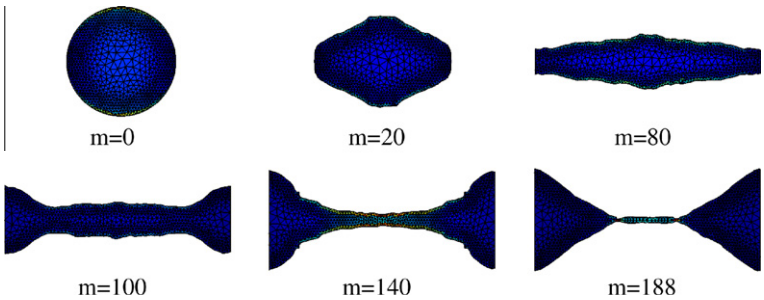

Fig. 12. The snapshots of structures in the optimization (Case 5).

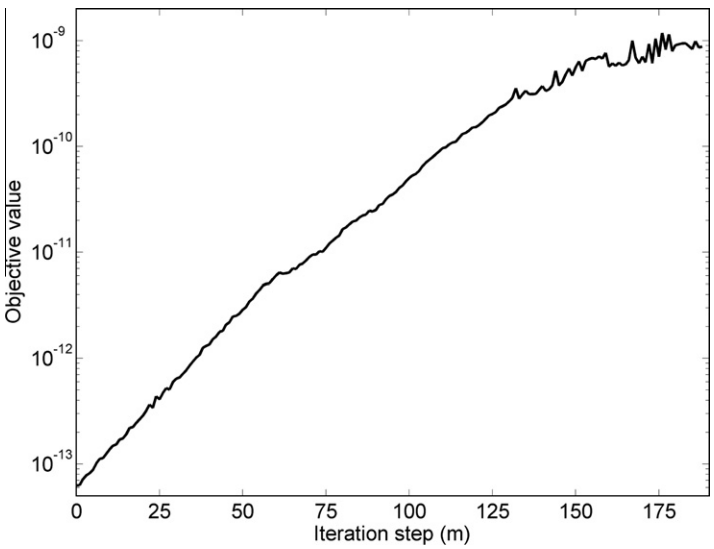

Fig. 13. The history of the objective function with logarithmic scale in vertical axis (Case 5).

history is plotted in a logarithmic axis to provide a clear view of its change as in Fig. 13. It distinctly shows the objective function continuously increasing in the beginning and intermediate stages. While in the final stage, it fluctuates slightly as the middle part of the structure tends to become as thin as possible but it is restricted by a limited mesh size. Such a fluctuation indicates that, compared with the self-adjoint example, the objective function appears more sensitive to a perturbation to the shape of the solid phase.

For comparative purposes, another non-self-adjoint case (Case 6) is presented with the similar initial structure (a square with four circular holes) to the self-adjoint design (Case 4). The snapshots in Fig. 14 illustrate that the holes break in the beginning of the optimization, shaping a fence-like structure with three vertical bars (m = 20–100 in Fig. 14). When the middle bump diminishes gradually (m = 180–240 in Fig. 14), we obtain a dumb-like structure with two elegant ends at iteration 330. Similarly to Case 5, the shape of the structure converges in the final stage (after iteration 300) while its middle part keeps evolving thinner and thinner.

4.3. The comparison of the results with traditional dipole antenna

Now that a number of dipole antennas are obtained from the optimization, we can compare their performance relative to the conventional designs in Fig. 1 with the same volume fraction. Fig. 15 shows the mean current density with respect to

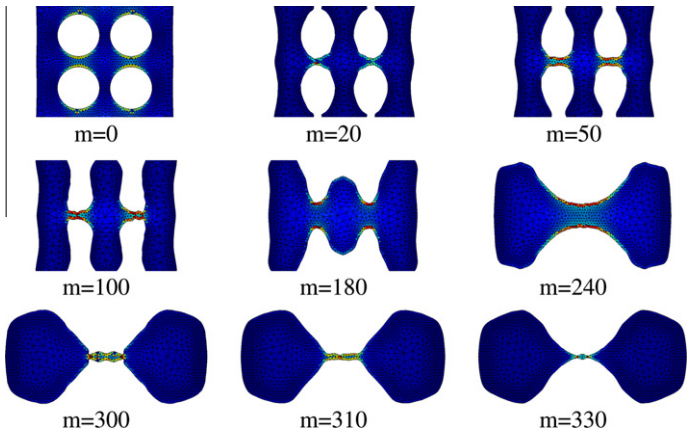

Fig. 14. The snapshots of structures in the optimization (Case 6).

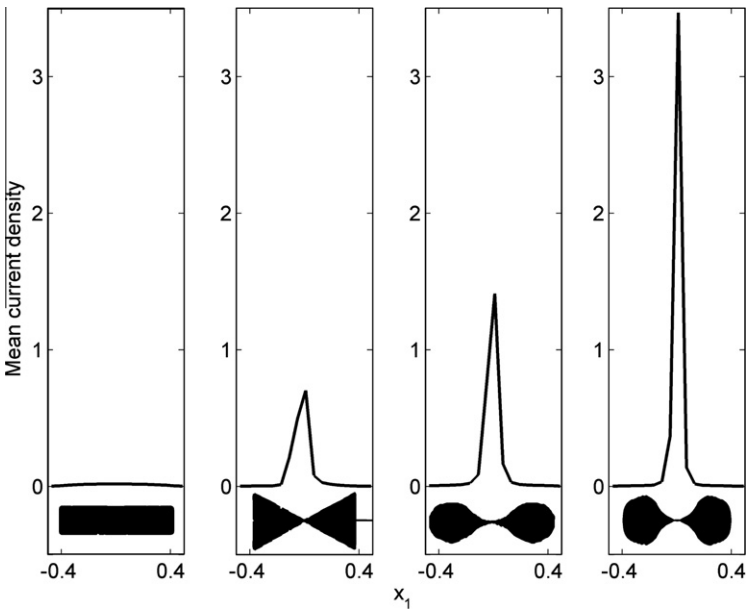

Fig. 15. The mean current density distribution with respect to the depth along horizontal direction for rod, triangular, tapered and our design antennas with the same volume fraction.

their depth along the horizontal direction for the rod, triangular, tapered and one of our non-self-adjoint designs (Fig. 14, $m = 300$) antennas from left to right, respectively. Except for the rectangular rod antenna whose density distribution is almost flat along horizontal direction, the rests have a peak corresponding to their middle notched shapes. Obviously, the optimized design presented herein provides the highest peak, which indicates that it has the best performance in terms of the maximal current density.

It should be pointed out, however, that the current density may not be the only way to formulate the objective for antenna design problems. Nevertheless, it is expected that the presented method provides a fundamental framework aiming to accommodate other antenna design problems.

5. Concluding remarks

This paper attempted to develop a level-set framework for electromagnetic topology optimization problems. The design of the dipole antenna is exemplified as a benchmark to validate the proposed level-set procedure. Specifically, solid (metal) boundaries are implicitly represented by the zero-level contour of a higher-dimensional scalar level-set function. To formulate a design objective for antenna design, the surface current flow, induced by the electric component of the incident wave, is calculated by solving the EFIE system. Thus, an integral form of current density over the solid phase is taken as a measure of antenna performance.

Based on the adjoint variable method and shape derivative, the sensitivity of the objective function is derived and used as the normal velocity for evolving the level-set model. With such normal velocity, the vacuum/metal interface gradually moves toward an optimum. In this paper, both the self-adjoint and non-self-adjoint examples with a number of design cases starting from different initials are presented to demonstrate the maximization of objective functions. The topology optimization clearly derives the shape with the highest current density. Thus, the voltage feeding can be placed to such a part so that the metal strip can be converted to a true dipole antenna. Compared with conventional design of dipole antennas, the optimized design appears to provide the highest current density.

As a first attempt, only the electric component of the incident wave is considered in this paper. The future study will take into account the magnetic component governed by the Maxwell's equations. Such an extension can be used for other more interesting yet more sophisticated electromagnetic applications, such as the design of metamaterials [25]. Since the technical details in the context are applicable to three-dimensional (3D) problems straightforward, they are not included in this paper but can be addressed in the future.

Acknowledgments

This study is supported by Australian Research Council (ARC) and the first author wishes to appreciate the support from the open fund (30915002) in the State Key Laboratory of Advanced Technology for Vehicle Design and Manufacture, Hunan University, China.

References

[1] R.F. Harrington, Field Computation by the Moment Methods, IEEE Press, New York, 1993.
[2] J.M. Jin, V. Liepa, Simple moment method program for computing scattering from complex cylindrical obstacles, IEE Proceedings-H: Microwaves, Antennas and Propagation 136 (1989) 321–329.
[3] K. Yee, Numerical solution of initial boundary value problems involving Maxwell' s equations in isotropic media, IEEE Transactions on Antennas and Propagation 14 (1966) 302–307.
[4] C.A. Balanis, Antenna Theory Analysis and Design, John Wiley & Sons, New Jersey, 2005.
[5] A.W. Maue, On the formulation of a general scattering problem by means of an integral equation, Zeitschrift fur Physik 126 (1949) 601–618.
[6] T.A. Milligan, Modern Antenna Design, John Wiley & Sons, New Jersey, 2005.
[7] G. Kiziltas, D. Psychoudakis, J.L. Volakis, N. Kikuchi, Topology design optimization of dielectric substrates for bandwidth improvement of a patch antenna, IEEE Transactions on Antennas and Propagation 51 (2003).
[8] T. Nomura, K. Sato, K. Taguchi, T. Kashiwa, S. Nishiwaki, Structural topology optimization for the design of broadband dielectric resonator antennas using the finite difference time domain technique, International Journal for Numerical Methods in Engineering 71 (2007) 1261–1296.
[9] M. Zhou, G.I.N. Rozvany, The COC algorithm. 2. Topological, geometrical and generalized shape optimization, Computer Methods in Applied Mechanics and Engineering 89 (1991) 309–336.
[10] M.P. Bendsøe, O. Sigmund, Topology Optimisation: Theory, Methods, and Applications, Springer, Berlin, NY, 2003.
[11] M.Y. Wang, S. Zhou, H. Ding, Nonlinear diffusions in topology optimisation, Structural and Multidisciplinary Optimization 28 (2004) 262–276.
[12] V.G. Veselago, The electrodynamics of substances with simultaneously negative values of ε and μ, Soviet Physics USPEKI 10 (1968) 509–514.
[13] S.W. Zhou, Q. Li, The relation of constant mean curvature surfaces to multiphase composites with extremal thermal conductivity, Journal of Physics D-Applied Physics 40 (2007) 6083–6093.
[14] Q. Li, G.P. Steven, O.M. Querin, Y.M. Xie, Shape and topology design for heat conduction by evolutionary structural optimisation, International Journal of Heat and Mass Transfer 42 (1999) 3361–3371.
[15] G.P. Steven, Q. Li, Y.M. Xie, Evolutionary topology and shape design for general physical field problems, Computational Mechanics 26 (2000) 129–139.
[16] S.W. Zhou, W. Li, Q. Li, Design of three-dimensional periodic metamaterials for electromagnetic properties, IEEE Transactions on Microwave Theory and Techniques 58 (2010) 910–916.
[17] Y.M. Xie, G.P. Steven, A simple evolutionary procedure for structural optimization, Computers and Structures 49 (1993) 885–896.
[18] S. Osher, J.A. Sethian, Front propagating with curvature dependent speed: algorithms based on Hamilton–Jacobi formulations, Journal of Computational Physics 78 (1988) 12–49.
[19] D.L. Chopp, Computing minimal-surfaces via level set curvature flow, Journal of Computational Physics 106 (1993) 77–91.
[20] J.A. Sethian, P. Smereka, Level set methods for fluid interfaces, Annual Review of Fluid Mechanics 35 (2003) 341–372.

[21] M. Burger, S.J. Osher, A survey on level set methods for inverse problems and optimal design, European Journal of Applied Mathematics 16 (2005) 263–301.
[22] G. Allaire, F. Jouve, A.M. Toader, Structural optimization using sensitivity analysis and a level-set method, Journal of Computational Physics 194 (2004) 363–393.
[23] J.A. Sethian, A. Wiegmann, Structural boundary design via level set and immersed interface methods, Journal of Computational Physics 163 (2000) 489–528.
[24] M.Y. Wang, X.M. Wang, D.M. Guo, A level set method for structural topology optimization, Computer Methods in Applied Mechanics and Engineering 192 (2003) 227–246.
[25] S.W. Zhou, W. Li, G.Y. Sun, Q. Li, A level-set procedure for the design of electromagnetic metamaterials, Optics Express 18 (2010) 6693–6702.
[26] O. Dorn, D. Lesselier, Level set methods for inverse scattering, Inverse Problems 22 (2006) R67–R131.
[27] L. He, S. Kindermann, M. Sini, Reconstruction of shapes and impedance functions using few far-field measurements, Journal of Computational Physics 228 (2009) 717–730.
[28] F. Murat, S. Simon, Etudes de problems d'optimal design, Lectures Notes in Computer Science 41 (1976) 54–62.
[29] S.J. Osher, J.A. Sethian, Front propagating with curvature dependent speed: algorithms based on Hamilton–Jacobi formulations, Journal of Computational Physics 78 (1988) 12–49.
[30] B. Delaunay, Sur la sphère vide, Izvestia Akademii Nauk SSSR, Otdelenie Matematicheskikh i Estestvennykh Nauk 7 (1934) 793–800.
[31] P.O. Persson, G. Strang, A simple mesh generator in MATLAB, SIAM Review 46 (2004) 329–345.
[32] M. Sussman, P. Smereka, S. Osher, A level set approach for computing solutions to incompressible 2-phase flow, Journal of Computational Physics 114 (1994) 146–159.
[33] A.W. Glisson, On the Development of Numerical Techniques for Treating Arbitrarily-Shaped Surfaces, University of Mississippi, 1978.
[34] S.M. Rao, D.R. Wilton, A.W. Glisson, Electromagnetic scattering by surfaces of arbitrary shape, IEEE Transactions on Antennas and Propagation AP-30 (1982) 409–418.
[35] S.W. Zhou, Q. Li, A variational level set method for the topology optimization of steady-state Navier–Stokes flow, Journal of Computational Physics 227 (2008) 10178–10195.
[36] Y. Jung, K.T. Chu, S. Torquato, A variational level set approach for surface area minimization of triply-periodic surfaces, Journal of Computational Physics 223 (2007) 711–730.
[37] S.Y. Wang, K.M. Lim, B.C. Khoo, M.Y. Wang, An extended level set method for shape and topology optimization, Journal of Computational Physics 221 (2007) 395–421.
[38] O. Sigmund, A 99 line topology optimization code written in Matlab, Structural and Multidisciplinary Optimization 21 (2001) 120–127.
[39] S.N. Makarov, Antenna and EM Modelling with Matlab, John Wiley & Sons, New York, 2002.